Brian Fischer

The Challenges of Measuring Integrated Antennas at Millimeter-Wave Frequencies

Linus Boehm, Frank Boegelsack, Martin Hitzler, and Christian Waldschmidt

EDITOR'S NOTE

The accurate measurement of millimeter-wave antennas is challenging, particularly in the presence of integrated electronics. Fortunately, modern robotic technology offers a highly accurate solution to the placement of measurement sensors. This issue's "Measurements Corner" column highlights a test apparatus composed of a robotic positioner and an ancillary laser sensor to measure the pattern of an integrated antenna at frequencies as high as 280 GHz. Following best practices, measurement uncertainty associated with known position accuracy and other factors is estimated.

The increasing demand for radar sensors and the wide distribution of handheld communication devices push the development of low-cost components with a small form factor. One approach to achieve smaller, low-cost devices is the integration of the required components on a monolithic microwave-integrated circuit (MMIC). At frequencies above 100 GHz, passive components are small enough to be integrated onto a chip, and the advances in semiconductor technology make it possible to build active components that can operate at millimeter (mm)-wave frequencies [1], [2]. The available bandwidths of several gigahertz at mm-wave frequencies offer high data rates for communication devices or high resolution for remote-sensing applications. By integrating the radio-frequency (RF) components and the antennas, lossy off-chip transitions can be avoided, thus limiting the required connections to the power supply and baseband signals.

While the realizability of communication and radar MMICs has been demonstrated [3]–[6], performance can still be improved. To transmit and receive signals, attuned antennas with specific radiation characteristics for the respective application are required, and to optimize the antennas, accurate and reliable measurement results are needed. For gain and efficiency measurements, the input power of the antenna under test (AUT) must be known. When used in a system, the input power to the antenna can only be measured over a coupler and an integrated power meter, which usually have a high uncertainty at mm-wave frequencies. Another approach is to measure the antenna by itself, outside the system, in which case wafer probes have to be used to contact the antenna [7]. This allows us to determine the input power with higher accuracy, and it also makes it possible to feed antenna prototypes without requiring active circuitry on the chip.

The measurements of the antennas proved to be challenging for various reasons:

- With wavelengths of around 1 mm, small deviations of the measurement position or misalignment of the setup cause amplitude and phase errors.
- Due to the small dimensions on a chip and the high integration level, it is not possible to probe signals other than the input and output signals.
- Wafer probes cause reflections in far-field measurements [8] and limit the scanning area for near-field measurements, as they are in close proximity to the AUT and orders of magnitude bigger.
- Parasitic wafer probe radiation superimposes with the AUT radiation and distorts the results [9].

Digital Object Identifier 10.1109/MAP.2017.2706652
Date of publication: 4 August 2017

- The measurement setups themselves distort the signals and create reflections and interference.
- Bending and movement of RF cables change their electrical characteristics and influence the measured signal.
- Small wavelengths make the construction of different components like probe antennas and connectors challenging.
- Measurement techniques used at lower frequencies like the Wheeler cap method [10], [11] are difficult to realize for the small dimensions on a chip and are often unstable across multiple frequencies.

For accurate measurements, setups must be sturdy, precise, minimally reflective, and steady over different factors like position and frequency. Furthermore, measurement setups have to be flexible and adaptable to support various antenna configurations for multiple measurement scenarios. This allows the investigation of different aspects of the antenna performance [12].

Different measurement setups have been presented to meet these requirements. The first setups for three-dimensional (3-D) radiation pattern measurements of integrated antennas used two rotary joints to move the receiving antenna on a spherical surface around the AUT [13], [14]. The setup in [13] was later extended for frequencies up to 325 GHz [15]. More recent setups focused on a higher positional accuracy [16] and minimal reflections [17], [18]. The setups in [14], [17], and [18] were designed for frequencies around 60 GHz, and the setup in [16] was designed for frequencies up to 110 GHz.

In [19]–[21], planar scans of the radiated near field are performed at around 100 GHz. However, due to the wafer probe, which is located right next to the AUT, the near-field scanning range is limited as shown in Figure 1. This hampers integrated antenna measurements in particular as the wide beamwidth requires a large scanning area to take into account as much of the radiated fields as possible for an accurate near-field to far-field transformation. While this signal truncation is not as critical in the plane orthogonal to the probe (x-z-plane in Figure 1), it severely distorts the calculated far field in probe direction (y-z-plane). The same is true for far-field measurements, where the distortion in the y-z-plane is caused by probe reflections when measuring with standard wafer probes.

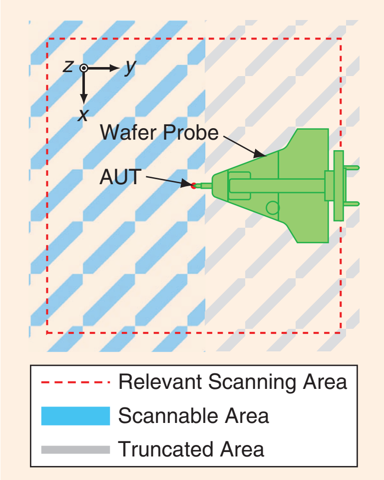

FIGURE 1. The wafer probe limits the scannable area for near-field scans. (Figure courtesy of Ulm University, Germany.)

A different approach was taken by [22], where a robotic arm is used to move the Rx antenna on the desired trajectory around the AUT to measure the radiated fields. This offers high flexibility in terms of size, position, and orientation of the AUT as well as in terms of scanning geometry, as the movements of the robot can be adjusted to changing measurement conditions by software.

The setup used in this article also uses a robotic arm to move the Rx antenna; however, to be able to measure integrated antennas, a probe station is used to contact integrated circuits on a chip. With the robotic arm, both near- and far-field measurements can be performed, as well as polarization and extrapolation measurements. The measurement is adaptable to many different antenna types and measurement scenarios with high precision.

MEASUREMENT SETUP OVERVIEW

A block diagram of the setup is shown in Figure 2. After a measurement was initiated, the control computer sends the measurement type, velocity, acceleration, movement limits, and resolution to the robot controller. The measurement frequency and resolution bandwidth are sent to the vector network analyzer (VNA), which is triggered by the robot whenever a measurement position is reached. Two different measurement modes are supported. During on-the-fly measurements, the robot moves with constant speed and the measurements are performed while moving. For point-to-point measurements, the robot stops at every measurement point, triggers the VNA after a specified wait time, and continues to the next point after the measurement was performed. For on-the-fly measurements, the measurement trajectory has to be run through once for every frequency, which is why point-to-point measurements are preferable for wide-band measurements, while being slower for single-frequency measurements. A graphical user interface is used to align the AUT and RX antenna, to adjust all

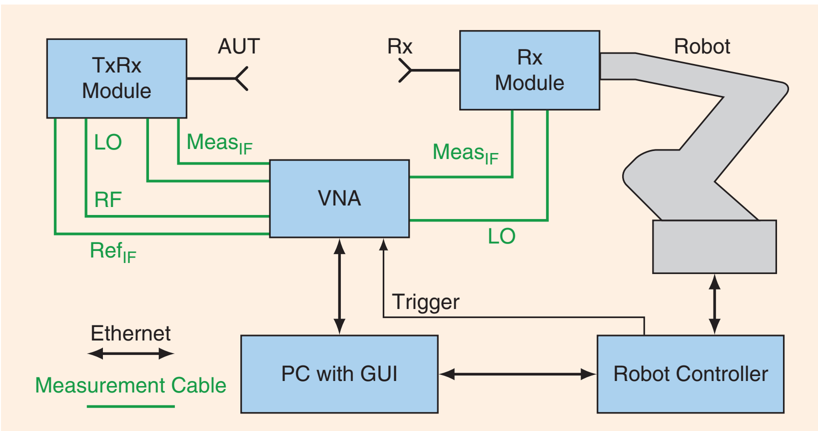

FIGURE 2. A schematic of the measurement setup. LO: local oscillator; PC: personal computer; GUI: graphical user interface. (Figure courtesy of Ulm University, Germany.)

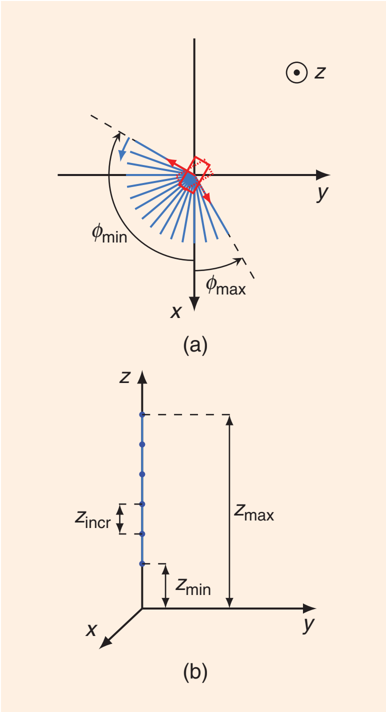

FIGURE 3. Polarization and extrapolation measurements. (a) The Rx antenna rotates around the z axis during a polarization measurement. (b) The radiation measurement for different AUT to Rx antenna separation distances. (Figure courtesy of Ulm University, Germany.)

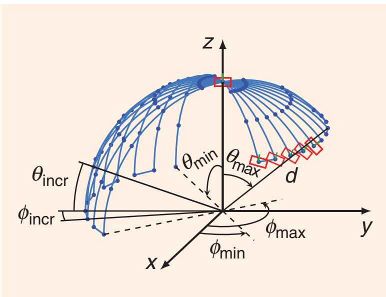

FIGURE 4. A far-field scan trajectory. (Figure courtesy of Ulm University, Germany.)

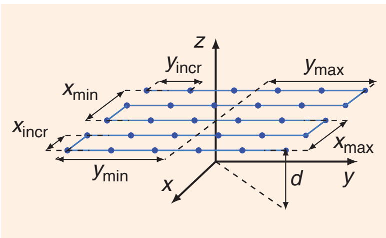

FIGURE 5. A near-field scan trajectory. (Figure courtesy of Ulm University, Germany.)

settings for the different measurement scenarios, and to initiate a measurement.

Near-field, far-field, extrapolation, and polarization scan measurements can be performed. During a polarization scan, the Rx antenna is centered over the AUT and rotated around the azimuth angle to determine the received field over ϕ [Figure 3(a)]. The cross-polarization angle can then be determined by finding the angle for which the received field has the minimum value. As the maximum is usually not as well defined, the copolarization angle is calculated with $\theta_{\text{co-pol}} = \theta_{\text{cross-pol}} \pm 90^{\circ}$. After $\theta_{\text{co-pol}}$ and $\theta_{\text{cross-pol}}$ have been determined, an automatic alignment for co- and cross-polarization measurements can be chosen for all measurement types. During an extrapolation measurement [Figure 3(b)], the radiated field is measured over the separation between the AUT and Rx antenna, which can be used to analyze the influence of reflections.

For far-field measurements, a minimum, maximum, and increment for ϕ (azimuth) and θ (elevation) angles must be chosen, as displayed in Figure 4. An arbitrary polarization (e.g., E_{ϕ}, E_{θ}, co/cross-polarization) can be chosen. To maintain the correct Rx antenna orientation for co/cross-polarization measurements, the antenna is rotated around its axis in between two cuts, as indicated in Figure 4. After a far-field measurement, an automatic AUT phase center determination can be performed, which can then be used as the measurement origin for subsequent measurements [23]. For planar near-field measurements, the start and stop value as well as the increment for the x and y range have to be specified (see Figure 5).

COMPONENTS

The setup is shown in Figure 6. The different components are explained next.

ROBOT

The robot has six degrees of freedom, a positional accuracy of 350 μm, and a repeatability of 50 μm. Two-dimensional cuts can be performed for θ-ranges over $\pm 90^{\circ}$. When measuring 3-D patterns, the maximum θ-angle depends on the measurement distance. For a distance of 150 mm, the maximum θ-range is over $\pm 90^{\circ}$, and for a distance of 250 mm, the maximum range is around $\pm 60^{\circ}$.

PROBE STATION

The probe station is required to contact integrated antennas and has a modular setup. Positioners, microscope, and chuck can be moved or removed depending on the measurement setup to minimize reflective surfaces. For integrated antenna measurements, a custom-made plastic chuck is used, which significantly reduces reflections [24].

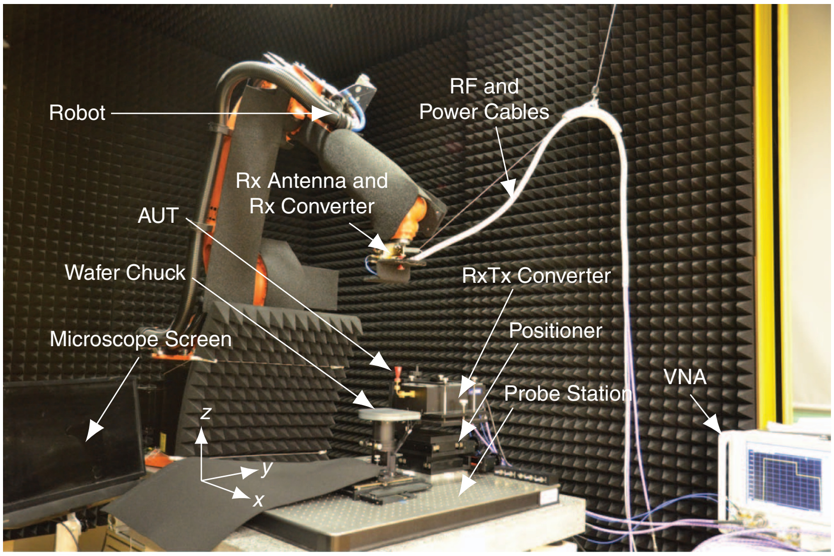

FIGURE 6. A measurement setup with components. (Photo courtesy of Ulm University, Germany.)

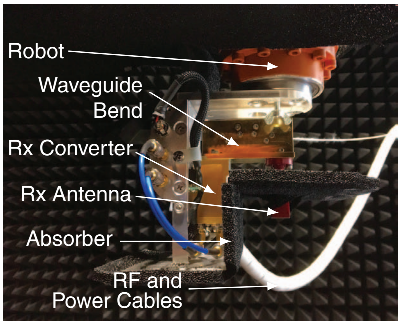

FIGURE 7. An Rx converter mount with an Rx antenna. (Photo courtesy of Ulm University, Germany.)

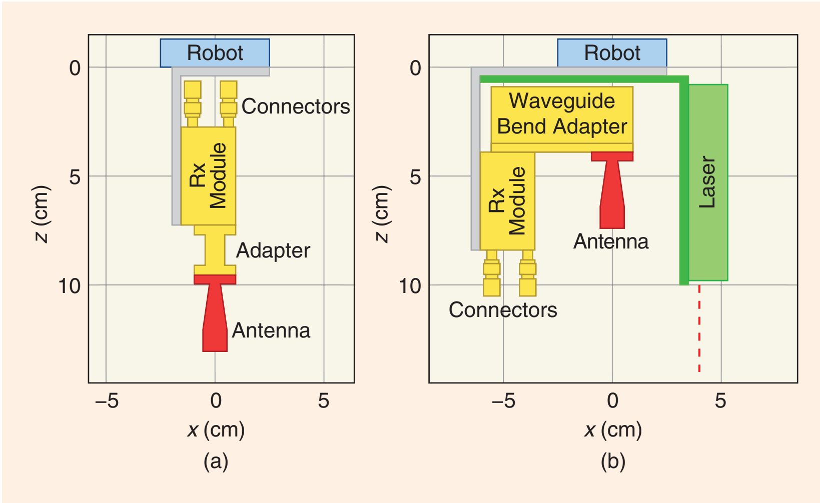

FIGURE 8. A comparison of Rx module-mounting structures: (a) a mounting structure without the waveguide bend and (b) a mounting structure with the waveguide bend and removable laser range finder. (Figure courtesy of Ulm University, Germany.)

MEASUREMENT EQUIPMENT

Measurements are taken with a VNA and appropriate converter modules for the different frequency ranges. For frequencies above 60 GHz, the AUT is fed with an RxTx converter module, and the signal received by the Rx antenna is fed to an Rx converter module, which is mounted to the robot as shown in Figure 7. A 180° waveguide bend is used to connect the Rx antenna with the Rx module. Figure 8 shows the mounting structure with and without the waveguide bend. Without the bend [Figure 8(a)], the distance between the Rx antenna aperture and the robot is about 13 cm. When using the waveguide bend as shown in Figure 8(b), the distance decreases to 7 cm, which allows for larger scanning angles. During a measurement, the mounting structure is covered with absorbers to reduce reflections.

Cables with a high phase stability are used to connect the converter modules to the VNA, and a spring balancer ensures minimum stress and bending during a measurement. The maximum phase error, measured on 15 cm × 15 cm planar scan area in the x-y-plane (see Figure 6) is $<3°$ at 160 GHz.

Wafer probes designed to contact integrated antennas up to 325 GHz are available. As chip sizes are small, the distance between probe tip and the AUT is usually smaller than 1 mm. The probe body of standard wafer probes presents a comparatively large reflective surface in the direct vicinity of the AUT. To reduce reflection, a special probe with an extended probe tip was designed (Figure 9) for the frequency range of 140–220 GHz (WR5.1) to increase the distance between probe and the AUT.

LASER RANGE FINDER

For the Rx AUT alignment, a laser distance meter can be attached to the robot as shown in Figure 8(b). The laser beam must then be centered over the AUT using the graphical user interface. Once the laser points on the AUT, the distance can be measured. With the distance between laser and the AUT, the current robot position and the relative distance between laser, AUT, and robot, the position of the AUT is calculated and used as the origin for measurements. The laser and its mounting structure [see Figure 8(b)] are removed during the measurement.

HORN ANTENNA MEASUREMENTS

To optimize the measurement setups, different absorber placements and cable routings were analyzed. Measurements were performed at 280 GHz with a horn antenna as the AUT. Figure 10 shows a comparison between a measurement without any absorbers and a measurement where the robotic arm and the probe station were covered with absorbers. The absorbers reduced reflections around the maximum of the antenna pattern and for angles $\theta > 0°$, where the arm of the robot was over the AUT [25].

With optimized cable routing and additional absorbers around the Rx antenna as shown in Figure 7, the deviations between measurement and simulation results are <5 dB within 40° of the main lobe as shown in Figure 11. The occurring deviations are mostly caused by production tolerances of the antenna rather than measurement errors. The production tolerances manifest themselves in the asymmetry between negative and positive θ-angles in the H-plane measurement, while the simulation is symmetrical. If the AUT is rotated by 180° around the z axis (see Figure 4), the measurement result is the mirrored result of Figure 11, which shows that the asymmetry is not due to a measurement error. Ripples caused by reflections can only be seen for relative amplitudes smaller than –60 dB. Figure 12 shows a 3-D measurement of the same horn antenna.

As mentioned in the "Measurement Setup Overview" section, planar near-field measurements can be performed. Figure 13 shows the result of a near- to far-field transformation of a horn antenna at 160 GHz in the H-plane. The measurement distance for the planar near-field measurement was 30 mm, and the sample spacing in x and y direction

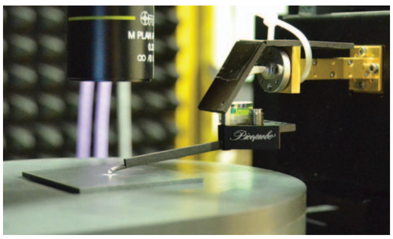

FIGURE 9. Contacting the AUT with wafer probe and microscope. (Photo courtesy of Ulm University, Germany.)

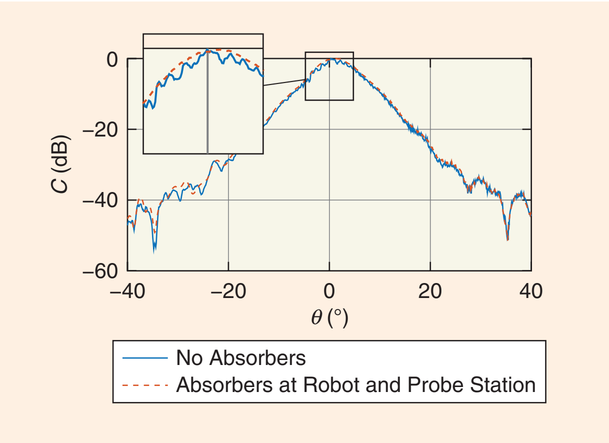

FIGURE 10. The influence of absorbers on the measured antenna pattern. (Figure courtesy of Ulm University, Germany.)

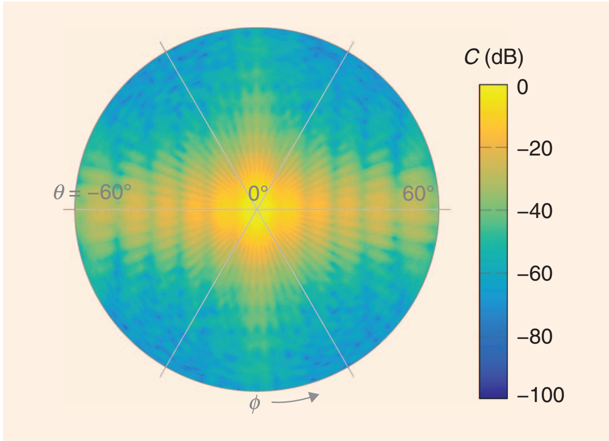

FIGURE 12. A 3-D measurement of a horn antenna at 280 GHz. (Figure courtesy of Ulm University, Germany.)

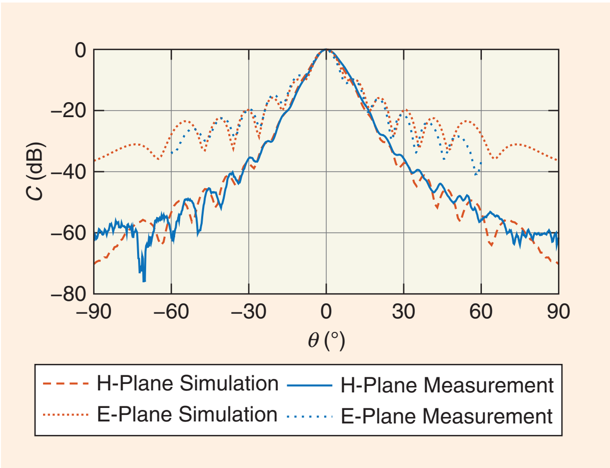

FIGURE 11. A measurement of a horn antenna at 280 GHz. (Figure courtesy of Ulm University, Germany.)

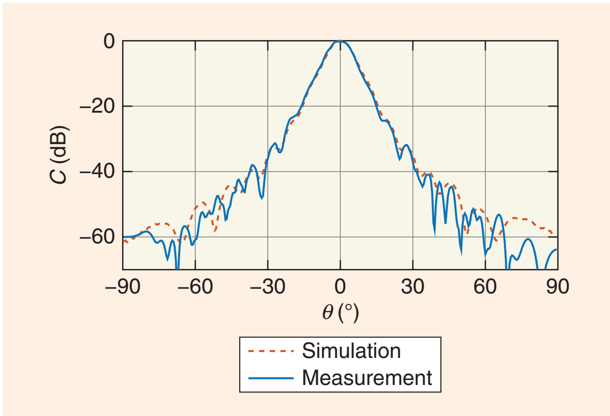

FIGURE 13. The near- to far-field transformation result (H-plane) of a planar near-field measurement of a horn antenna at 160 GHz. The measurement distance was 30 mm. (Figure courtesy of Ulm University, Germany.)

was $x_{\text{incr}} = y_{\text{incr}} = 0.5$ mm. While this demonstrates the viability of near-field measurements with the setup, no probe or position correction measures were applied, which explains why the measurements deviate from the simulation results for $\theta > 30^\circ$.

UNCERTAINTY BUDGET

To quantify the overall accuracy of the measurement setup, an error analysis as explained in [26] was performed, and the uncertainty budgets for radiation pattern, directivity, and gain measurements for integrated antennas were calculated at 160 GHz.

The uncertainty budget was determined with

$$U_c(y) = k\sqrt{\sum_{i=1}^{N}(c_i \cdot s_{x_i})^2}. \qquad (1)$$

In (1), s_{x_i} is the standard deviation of a certain error source x_i, and c_i is the sensitivity of the measurement result toward this error source. The total number of considered uncertainties is denoted by N, and k is the coverage factor, which was set to $k = 2$ in this case to correspond to a 95% confidence. We assumed that the error sources follow a normal distribution, in which case the standard deviation of an error source can be calculated with [26]

$$s_{x_i} = \frac{1}{3}u(x_i), \qquad (2)$$

where $u(x_i)$ is the maximum deviation.

The impact of the identified error sources, listed in Table 1, on the measurement results was analyzed for radiation pattern, directivity, and gain measurements to calculate the overall measurement uncertainty.

A version of the 280-GHz integrated antenna shown in Figure 14 was scaled to 160 GHz and used as an AUT for all measurements. The microstrip feeding line coupled in a substrate-integrated resonator, which then coupled in a dielectric resonator that was glued on the chip [27].

RADIATION PATTERN

A comparison between the measured and simulated radiation patterns is shown in the H- and E-planes in Figure 15. Good agreement with the simulation results is achieved in both planes with deviations of <1.5 dB in the H-plane and <2 dB in the E-plane for θ-angles within 60° of the main lobe. Deviations can be due to production tolerances, e.g., misalignment of the dielectric resonator.

TABLE 1. UNCERTAINTY BUDGETS.

#	Source of Uncertainty x_i	Affected Measurements	Uncertainty $(\pm)\,u(x_i)$	Radiation Pattern		Directivity		Gain	
				c_i	s_{xi}	c_i	s_{xi}	c_i	s_{xi}
1	AUT pos x	RP/D/G	1.5 mm	0.072 dB/mm	0.5 mm	0.002 dB/mm	0.5 mm	0.048 dB/mm	0.5 mm
2	AUT pos y	RP/D/G	1.5 mm	0.100 dB/mm	0.5 mm	0.004 dB/mm	0.5 mm	0.04 dB/mm	0.5 mm
3	AUT pos z	RP/D/G	2.0 mm	0.127 dB/mm	0.67 mm	0.001 dB/mm	0.67 mm	0.063 dB/mm	0.67 mm
4	AUT phase center	RP/D/G	1.0 mm	0.034 dB/mm	0.03 mm	0.001 dB/mm	0.03 mm	0.027 dB/mm	0.33 mm
5	AUT tilt	RP/D/G	0.125°	0.2 dB/°	0.042°	≈ 0	—	0.01 dB/°	≈ 0
6	AUT mismatch	G		—	—	—	—	≈ 0	—
7	Rx tilt	—	0.1°	—	—	—	—	—	—
8	Rx length	—	100 μm	—	—	—	—	—	—
9	Rx phase center	—	5.0 mm	—	—	—	—	—	—
10	Rx gain	—	0.2 dB	—	—	—	—	—	—
11	REF gain	G	0.4 dB	—	—	—	—	1	0.13 dB
12	REF tilt	G	0.125°	—	—	—	—	1.37 dB/°	0.04°
13	REF phase center	G	5.0 mm	—	—	—	—	0.015 dB/mm	2.33 mm
14	REF mismatch	G		—	—	—	—	≈ 0	—
15	Connectors	G	0.4 dB	—	—	—	—	1 dB/dB	0.53 dB
16	Trigger position	RP	350 μm					—	—
17	Cable flex	RP						—	—
18	Noise	RP/G		1 dB/dB	0.04 dB	1 dB/dB	0.01 dB	1 dB/dB	0.09 dB
19	AUT-Rx-polarization	RP/D/G	0.1°	—	≈ 0	—	≈ 0	—	≈ 0
20	Distance	G	350 μm	—	—	—	—	≈ 0	≈ 0
21	Reflections	RP/D/G		1 dB/dB	0.04 dB	1 dB/dB	0.02 dB	1 dB/dB	0.04 dB
22	ϕ resolution (4°)	D		—	—			—	—
23	θ resolution (0.5°)	RP/D		≈ 0	—	1 dB/dB	0.04 dB	—	—
24	Maximum-θ truncation	D		—	—	1 dB/dB	0.07 dB	—	—
25	VNA crosstalk	RP/D	112 nV_{rms}	—	≈ 0	—	≈ 0	—	≈ 0
26	Absorber placement	RP/D/G		—	≈ 0	—	≈ 0	—	≈ 0
27	Probe placement	RP/D/G		1 dB/dB	0.07 dB	—	≈ 0	—	≈ 0
28	Receiver nonlinearity	RP/D/G		1 dB/dB	0.05 dB	1 dB/dB	0.07 dB	—	≈ 0
29	Long-term effects	RP/D/G		1 dB/dB	0.03 dB	1 dB/dB	0.07 dB	1 dB/dB	0.33
Expanded uncertainty $U_c(y)$ (95% confidence):				0.3 dB		0.3 dB		1.3 dB	

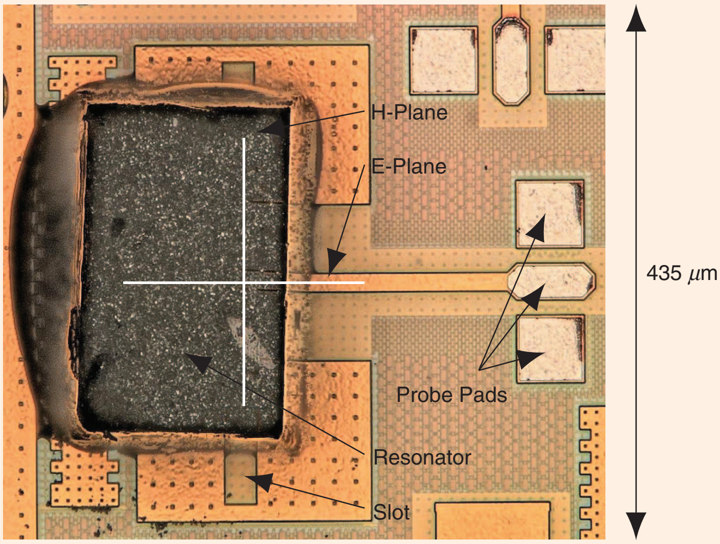

FIGURE 14. The integrated antenna at 280 GHz. (Photo courtesy of Ulm University, Germany.)

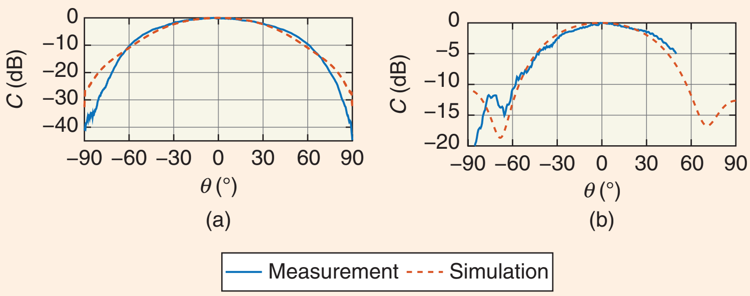

FIGURE 15. The (a) H-plane and (b) E-plane measurement of the integrated antenna at 160 GHz. (Figure courtesy of Ulm University, Germany.)

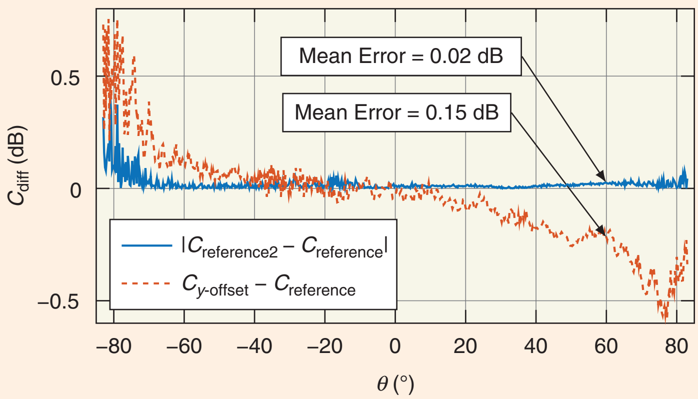

FIGURE 16. The deviation between two sets of reference measurements and between a *y*-offset and reference measurement. (Figure courtesy of Ulm University, Germany.)

The measured E-plane pattern has more ripples than the H-plane pattern, which is caused by reflections from the wafer probe. As the probe is connected in the E-plane (see Figure 14), the reflections from the probe surface create more distortions in the E-plane compared to the H-plane. Furthermore, the probe and the converter module block part of the area around the AUT and prevent the robot from measuring the complete upper hemisphere. The E-plane could therefore only be measured for $-90^\circ < \theta < 50^\circ$.

The radiation pattern uncertainty was evaluated in an interval within 30 dB of the main lobe, which almost covers the θ-angles from $-90^\circ < \theta < 90^\circ$.

The sensitivities were determined by comparing a reference measurement with an erroneous measurement, where one source of uncertainty was deliberately changed. When analyzing a specific error source, x_i, the effects of other error sources should be minimized. To make sure that random errors are not included in the calculation of the sensitivity toward x_i, ten measurements were averaged for the reference and the erroneous measurement. Figure 16 shows the calculated difference for two examples: the difference between two averaged reference measurements and between averaged reference measurements and measurements with an out-of-center AUT $C_{y\text{-offset}}$. The measurement was taken in the y-z-plane, and the AUT was moved in – y-direction. The results of $C_{y\text{-offset}}$ are therefore too high for negative θ values and too low for positive θ values. The mean error for the offset measurement is 0.15 dB and much higher than the deviation between the two reference measurements of 0.02 dB. The noise contribution to the measured error can therefore be neglected and the error can be fully attributed to the y offset.

The sensitivity toward a y offset can now be calculated with

$$c_{y\text{-offset}} = \frac{\text{mean error}}{y\text{-offset}} = \frac{0.15\ \text{dB}}{1.5\ \text{mm}} = 0.1\frac{\text{dB}}{\text{mm}}. \qquad (3)$$

The overall expanded uncertainty budget is 0.3 dB for radiation pattern

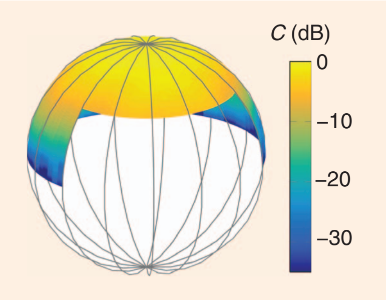

FIGURE 17. The covered measurement area. (Figure courtesy of Ulm University, Germany.)

measurements with a coverage factor of $k = 2$.

DIRECTIVITY

To determine the directivity of the AUT, a 3-D measurement over the radiated field was performed (see Figure 17). The directivity can be calculated by integrating over the normalized radiation pattern magnitude $C(\theta, \phi)$ on a sphere around the AUT:

$$D_i = \frac{4\pi}{\int_{\phi=0}^{\pi}\int_{\theta=-\pi}^{\pi} C^2(\theta,\phi)|\sin(\theta)|d\theta d\phi}. \quad (4)$$

Due to the integration, misalignment errors have a smaller impact compared to radiation pattern measurements. Furthermore, random errors are averaged by the integration leading to a smaller sensitivity toward noise and trigger position of 0.01 dB compared to 0.04 dB for radiation pattern measurements. As long as the ϕ- and θ-increments are not unreasonably large, the discrete integration has a small impact on the result. For these measurements the ϕ- and θ-increments were 4° and 0.5°, respectively.

For the directivity calculation, the field must be integrated over a full sphere around the AUT. Due to the probe station and the limited robot movements, the lower hemisphere cannot be measured. The RxTx converter module and the positioner (see Figure 6) block part of the upper hemisphere, which is why the hashed areas in Figure 18 also could not be measured. The error (#24 – maximum-θ truncation in Table 1) can be estimated by calculating boundary values for the directivity. If the areas that could not be measured are assumed to be zero [Figure 18(a)], the integral is underestimated, which leads to an upper bound of the directivity of 9.76 dBi. The estimated directivity was calculated by mirroring the measured field in the area, where no measurements could be taken as shown in Figure 18(b). Additionally, the field in the lower hemisphere was assumed to be the same as on the edges at $\theta = |90°|$. This results in a measured directivity of 9.54 dBi, which is very close to the simulated directivity of 9.47 dBi. The standard deviation of the maximum θ uncertainty is

$$s_{x\theta} = \frac{D_{\text{upper}} - D_{\text{meas}}}{3} = \frac{9.76 - 9.54}{3}\text{dB} = 0.07 \text{ dB}. \quad (5)$$

The expanded uncertainty for directivity measurements is 0.3 dB.

GAIN

The gain comparison method was used to determine the gain of the AUT. After measuring the S_{21} of a reference antenna, the gain of the AUT can be calculated with

$$G_{\text{AUT}}|_{\text{dBi}} = S_{21,\text{AUT}}|_{\text{dB}} - S_{21,\text{ref}}|_{\text{dB}} + G_{\text{ref}}|_{\text{dBi}} - S_{21,\text{con}}|_{\text{dB}}. \quad (6)$$

All connectors that differ between the two measurements are taken into account by $S_{21,\text{con}}$. In this case, the connectors were a 90° waveguide bend ($S_{21,\text{WGB}}$), which was used to connect the reference horn antenna, the wafer probe to contact the chip ($S_{21,\text{probe}}$), and the microstrip line on the chip itself ($S_{21,\text{chip}}$).

$$S_{21,\text{con}}|_{\text{dB}} = S_{21,\text{probe}}|_{\text{dB}} + S_{21,\text{chip}}|_{\text{dB}} - S_{21,\text{WGB}}|_{\text{dB}}. \quad (7)$$

The overall uncertainty budget for gain measurements is 1.3 dB, mainly caused by the high sensitivity toward faulty connector attenuations. The uncertainty is much higher compared to the radiation pattern and directivity uncertainty, but it is still reasonably good. A comparison between simulated and measured gain over frequency is shown in Figure 19.

CONCLUSIONS

We have described a highly flexible measurement setup for integrated antennas at frequencies above 100 GHz as well as its different components. Measurements of a horn antenna at 280 GHz closely matched the simulation results. Furthermore, we performed a thorough uncertainty analysis of a measurement setup for integrated antennas at 160 GHz. The calculated measurement uncertainty is below 0.3 dB for both radiation pattern

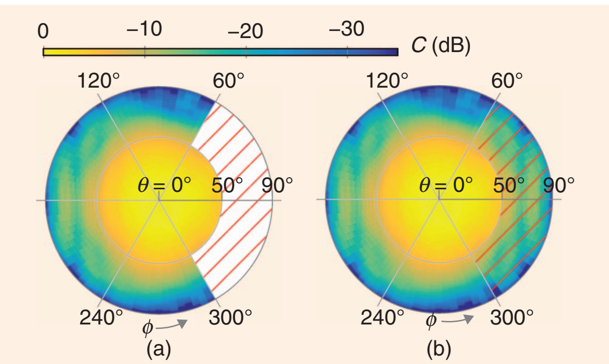

FIGURE 18. The measured radiation pattern of the integrated antenna at 160 GHz: (a) the upper bound for the directivity and (b) the estimated directivity. The wafer probe is located in the $\phi = 0°$ direction. (Figure courtesy of Ulm University, Germany.)

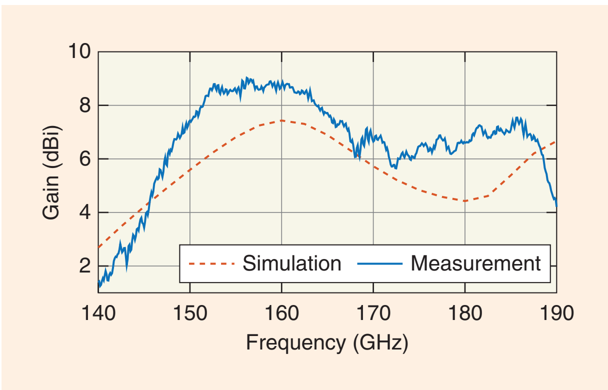

FIGURE 19. The simulated and measured gain of the integrated antenna at 160 GHz. (Figure courtesy of Ulm University, Germany.)

and directivity measurements. This small uncertainty is supported by the good agreement between measurement and simulation results. The maximum deviation for the radiation pattern was <2 dB for angles within $\theta < 60^\circ$ of the main lobe, and the difference between measured and simulated directivity was <0.1 dB. The uncertainty for gain measurements of 1.3 dB was higher. The main source of uncertainty was the connector, especially due to the high sensitivity of the measured gain toward inaccurate connector attenuations.

ACKNOWLEDGMENT

This work was supported by the German Research Foundation (DFG) under project number WA 3506/1–1.

AUTHOR INFORMATION

Linus Boehm (linus.boehm@uni-ulm.de) received his M.S. degree from Columbia University, New York, in 2013. In 2014, he joined the Institute of Microwave Engineering at Ulm University, Germany, where he is working toward his Ph.D. degree. His research focuses on minimizing errors in integrated antenna measurements above 100 GHz. He is a Student Member of the IEEE.

Frank Boegelsack (frank.boegelsack@uni-ulm.de) received his Dr.-Ing. degree from the University of Duisburg, Germany, in 1989. He is currently working on measurement setup development and millimeter-wave antenna measurements at the Institute of Microwave Engineering, Ulm University, Germany.

Martin Hitzler (Martin.Hitzler@uni-ulm.de) received his Dipl.-Ing. degree in electrical engineering from Ulm University, Germany, in 2012. In 2013, he joined the Institute of Microwave Engineering at Ulm University and is currently working toward his Ph.D. degree. His research interests include frequency-modulated continuous wave radar sensors, integrated antennas, and monolithic microwave integrated circuit packaging at millimeter-wave frequencies. He is a Student Member of the IEEE.

Christian Waldschmidt (christian.waldschmidt@uni-ulm.de) received his M.S. and Ph.D. degrees in electrical engineering from the University of Karlsruhe, Germany, in 2001 and 2004, respectively. He has been with Bosch since 2004, heading different research and development teams in microwave engineering. In 2013, he was appointed director of the Institute of Microwave Engineering at Ulm University, Germany, as a full professor. His research topics focus on radar, submillimeter-wave engineering, and antennas. He is a Senior Member of the IEEE.

REFERENCES

[1] G. Avenier, M. Diop, P. Chevalier, G. Troillard, N. Loubet, J. Bouvier, L. Depoyan, N. Derrier, M. Buczko, C. Leyris, S. Boret, S. Montusclat, A. Margain, S. Pruvost, S. T. Nicolson, K. H. K. Yau, N. Revil, D. Gloria, D. Dutartre, S. P. Voinigescu, and A. Chantre, "0.13 μm SiGe BiCMOS technology fully dedicated to mm-wave applications," *IEEE J. Solid-State Circuits*, vol. 44, pp. 2312–2321, Sept. 2009.

[2] H. Ruecker, B. Heinemann, and A. Fox, "Half-terahertz SiGe BiCMOS technology," in *Proc. IEEE 12th Topical Meeting Silicon Monolithic Integrated Circuits RF Syst. (SiRF)*, Jan. 2012, 133–136.

[3] M. Hitzler, S. Saulig, L. Boehm, W. Mayer, W. Winkler, and C. Waldschmidt, "Compact bistatic 160 GHz transceiver MMIC with phase noise optimized synthesizer for FMCW radar," *IEEE Int. Microwave Symp.*, May 2016.

[4] I. Sarkas, J. Hasch, A. Balteanu, and S. P. Voinigescu, "A fundamental frequency 120-GHz SiGe BiCMOS distance sensor with integrated antenna," *IEEE Trans. Microw. Theory Techn.*, vol. 60, pp. 795–812, Mar. 2012.

[5] N. Sarmah, J. Grzyb, K. Statnikov, S. Malz, P. R. Vazquez, W. Ferster, B. Heinemann, and U. R. Pfeiffer, "A fully integrated 240-GHz direct-conversion quadrature transmitter and receiver chipset in SiGe technology," *IEEE Trans. Microw. Theory Techn.*, vol. 64, pp. 562–574, Feb. 2016.

[6] H. J. Song, J. Y. Kim, K. Ajito, M. Yaita, and N. Kukutsu, "Fully integrated ASK receiver MMIC for terahertz communications at 300 GHz," *IEEE Trans. THz Sci. Techn.*, vol. 3, pp. 445–452, July 2013.

[7] R. Hahnel, B. Klein, C. Hammerschmidt, D. Plettemeier, P. V. Testa, C. Carta, and F. Ellinger, "Distributed on-chip antennas to increase system bandwidth at 180 GHz," in *Proc. 2016 German Microwave Conf. (GeMiC)*, Mar. 2016, pp. 161–164.

[8] L. Boehm, M. Hitzler, F. Roos, and C. Waldschmidt, "Probe influence on integrated antenna measurements at frequencies above 100 GHz," in *Proc. European Microwave Conf. (EuMC)*, London, U.K., Oct. 2016.

[9] J. Murdock, E. Ben-Dor, F. Gutierrez, and T. S. Rappaport, "Challenges and approaches to on-chip millimeter wave antenna pattern measurements," in *Proc. 2011 IEEE MTT-S Int. Microwave Symposium*, June 2011, pp. 1–4.

[10] E. Newman, P. Bohley, and C. Walter, "Two methods for the measurement of antenna efficiency," *IEEE Trans. Antennas Propag.*, vol. 23, pp. 457–461, July 1975.

[11] R. H. Johnston and J. G. McRory, "An improved small antenna radiation-efficiency measurement method," *IEEE Antennas Propag. Mag.*, vol. 40, pp. 40–48, Oct. 1998.

[12] D. Novotny, M. Francis, R. Wittmann, J. Gordon, J. Guerrieri, and A. Curtin, "Multi-purpose configurable range for antenna testing up to 220 GHz," in *Proc. 10th European Conf. Antennas and Propagation (EuCAP)*, Apr. 2016, pp. 4006–4008.

[13] S. Beer and T. Zwick, "Probe-based radiation pattern measurements for highly integrated millimeter-wave antennas," in *Proc. 4th European Conf. Antennas and Propagation (EuCAP)*, 2010, pp. 1–5.

[14] D. Titz, F. Ferrero, and C. Luxey, "Development of a millimeter-wave measurement setup and dedicated techniques to characterize the matching and radiation performance of probe-fed antennas [Measurements Corner]," *IEEE Antennas Propag. Mag.*, vol. 54, no. 4, pp. 188–203, 2012.

[15] H. Gulan, S. Beer, S. Diebold, C. Rusch, A. Leuther, I. Kallfass, and T. Zwick, "Probe-based antenna measurements up to 325 GHz for upcoming millimeter-wave applications," in *Proc. 2013 Int. Workshop on Antenna Technology (iWAT)*, pp. 228–231.

[16] F. Ferrero, S. Gregson, J. Lanteri, L. Brochier, Y. Benoit, C. Migliaccio, *and* J.-Y. Dauvignac, "Spherical near-field probe-fed antenna techniques for accurate millimeter wave measurements," in *Proc. 10th European Conf. Antennas and Propagation (EuCAP)*, Apr. 2016, pp. 4021–4024.

[17] A. Reniers, A. van Dommele, A. Smolders, and M. Herben, "The influence of the probe connection on mm-wave antenna measurements," *IEEE Trans. Antennas Propag.*, vol. 63, pp. 3819–3825, Sept. 2015.

[18] E. C. Lee, E. Szpindor, and W. E. McKinzie III, "Mitigating effects of interference in on-chip antenna measurements," in *Proc. AMTA 37th Annual Meeting and Symposium*, Long Beach, CA, Oct. 2015.

[19] G. Gentile, V. Jovanovic, M. Pelk, L. Jiang, R. Dekker, P. de Graaf, B. Rejaei, L. de Vreede, L. Nanver, and M. Spirito, "Silicon-filled rectangular waveguides and frequency scanning antennas for mm-wave integrated systems," *IEEE Trans. Antennas Propag.*, vol. 61, pp. 5893–5901, Dec. 2013.

[20] Z.-M. Tsai, Y.-C. Wu, S.-Y. Chen, T. Lee, and H. Wang, "A V-band on-wafer near-field antenna measurement system using an IC probe station," *IEEE Trans. Antennas Propag.*, vol. 61, pp. 2058–2067, Apr. 2013.

[21] K. A. Ladds, H. P. Nel, and T. Stander, "A novel e-band nearfield scanner for wafer probed on-chip antenna characterisation," in *Proc. 10th European Conf. Antennas and Propagation (EuCAP)*, Apr. 2016, pp. 1–4.

[22] J. A. Gordon, D. R. Novotny, M. H. Francis, R. C. Wittmann, M. L. Butler, A. E. Curtin, and J. R. Guerrieri, "Millimeter-wave near-field measurements using coordinated robotics," *IEEE Trans. Antennas Propag.*, vol. 63, no. 12, pp. 5351–5362, Dec. 2015.

[23] L. Boehm, F. Boegelsack, M. Hitzler, and C. Waldschmidt, "Enhancements in mm-wave antenna measurements: Automatic alignment and achievable accuracy," *IET Microwaves, Antennas & Propagation*, vol. 2, Feb. 2017.

[24] L. Boehm, M. Hehl, and C. Waldschmidt, "Influence of the wafer chuck on integrated antenna measurements," in *Proc. 2016 German Microwave Conf. (GeMiC)*, Mar. 2016, pp. 274–277.

[25] L. Boehm, S. Pledl, F. Boegelsack, M. Hitzler, and C. Waldschmidt, "Robotically controlled directivity and gain measurements of integrated antennas at 280 GHz," in *Proc. 2015 European Microwave Conf. (EuMC)*, Sept. 2015, pp. 315–318.

[26] NIST/SEMATECH. (June 2003). *e-Handbook of Statistical Methods* [Online]. Available: http://itl.nist.gov/div898/handbook/mpc/mpc.htm

[27] D. Hou, W. Hong, W. L. Goh, J. Chen, Y.-Z. Xiong, S. Hu, and M. Madihian, "D-Band on-chip higher-order-mode dielectric-resonator antennas fed by half-mode cavity in CMOS technology," *IEEE Antennas Propag. Mag.*, vol. 56, pp. 80–89, June 2014.